AIAA JOURNAL
Vol. 40, No. 3, March 2002

Dynamics of Slender Bodies Separating from Rectangular Cavities

V. I. Shalaev* and A. V. Fedorov†
Moscow Institute of Physics and Technology, Zhukovski, 14080, Russia
and
N. D. Malmuth‡
Rockwell Scientific Company, Thousand Oaks, California 91630

Vertical and pitching motions (two degrees of freedom) of a thin body of revolution separating from a rectangular cavity in a subsonic stream are investigated using combined asymptotic and numerical methods. The analysis is based on explicit analytical solutions for the lift force and pitching moment obtained in our previous studies. Body trajectory dependencies on initial conditions, body parameters, and freestream velocity are studied. The problem is divided into three phases of the motion. In phase 1, the body is inside the cavity. In phase 2, the body crosses the shear layer, and in phase 3, the body is outside the cavity. For phases 1 and 3, analytical solutions of the body dynamics are obtained for typical cases. This analysis provides insight into the separation process and identifies governing lumped nondimensional parameters relevant to the body dynamics as well providing a model that can provide quick, computationally non-intensive estimates of store separation with a personal computer. The role of the nondimensional parameters in the dynamic stability eigenvalues is identified and found particularly useful in this connection. These parameters implicitly contain the effect of the shear layer. Numerical calculations for all three phases are in good agreement with a major portion of the free-drop experimental data obtained in a subsonic wind tunnel. However, there are cases when the agreement is only satisfactory. The discrepancy is associated with a pitching bifurcation when the body crosses the shear layer. It is shown that small variation of the initial conditions can trigger quick transition from one pitch angle trajectory to another and cause dramatic changes of the body trajectory outside the cavity.

Nomenclature

$a(x)$	=	local body radius
a_0	=	maximum body radius
b_i	=	coefficient defined after Eqs. (4), $i = 1, 2$
b_{ij}	=	coefficient defined after Eqs. (4), $i, j = 1, 2$
c_g	=	gravity force coefficient (Froude number); Eq. (2c)
c_l	=	lift force apparent mass; Eq. (2c)
c_m	=	apparent pitch inertia; Eq. (2c)
G_1, G_2, G_3	=	coefficients defined in Eq. (3d)
g	=	gravity acceleration
$g_0,\ g_1,\ g_2$	=	body shape factors; Eq. (3c)
$H(X, t)$	=	vertical distance from body axis to slip surface
H_0	=	cavity depth
I	=	moment of inertia
L	=	lift force
l_0	=	body length
M	=	pitch moment
m	=	body mass
p	=	pressure
t	=	time
u, v, w	=	flow velocity components
V_a	=	defined in Eq. (2b)
V_r	=	characteristic vertical speed
V_0	=	body initial vertical speed; see Eq. (2d)
X, Y, Z	=	Cartesian laboratory frame with origin shown in Fig. 1a
X_c, Y_c, Z_c	=	Cartesian moving body axes with origin at body c.g.
x, y, z	=	Cartesian moving body axes at general location in body
α	=	pitch angle or angle of attack
$\alpha_{11}, \alpha_{12}, \alpha_{22}$	=	coefficients defined after Eq. (3)
γ	=	angular velocity stability parameter, $\mathrm{Re}(\lambda)$
$\Delta_1, \Delta_2, \Delta_3$	=	coefficients defined after Eqs. (4)
δ	=	body half-thickness ratio, $\hat{a}_0/\hat{l}_0$
θ	=	azimuth angle
λ	=	eigenvalue
ρ	=	density
Φ	=	near-field flow potential
Ω	=	angular frequency of body oscillations, $-\mathrm{Im}(\lambda)$
ω	=	pitch angular velocity
ω_a	=	defined in Eq. (2b)

Subscripts

a	=	body cross section of radius a
b	=	body surface
c	=	c.g.
e	=	body base
0	=	initial value
∞	=	freestream

Superscripts

$\wedge$	=	dimensional value
$+$	=	inside the cavity

Received 12 October 2000; presented as Paper 2001-2996 at the AIAA 31st Fluid Dynamics Conference, Anaheim, CA, 11–14 June 2001; revision received 3 September 2001; accepted for publication 3 September 2001.

*Associate Professor, Department of Aeromechanics and Flight Engineering.
†Associate Professor, Department of Aeromechanics and Flight Engineering. Member AIAA.
‡Senior Scientist, Department of Material Sciences. Fellow AIAA.

Introduction

MODELING of store separation from a cavity, even into a subsonic external stream is a very difficult problem that is the subject of the intensive application of current computational fluid

dynamics. The motivation of the work described herein is the need for quick methods for certification and assessment of the physics of store separation from cavities. Similar rapid evaluation methods are needed for stage and cargo separations. A variety of computational methods have been developed.[1–3] As contrasted to pure computational modeling, this paper discusses a combined asymptotic and numerical approach. It will be applied to solve aerodynamic problems relevant to separation of a thin body of revolution from rectangular cavities into subsonic or transonic flows.[4,5] The separation process can be divided into three phases. In phase 1, the body is inside the cavity. In phase 2, the body crosses the shear layer that separates the cavity flow from the external flow. In phase 3, the body is outside the cavity. In many practical cases, viscous effects can be approximated with inviscid models. As an example, a vortex sheet representing an infinitesimally thin slip surface can be used to approximate the shear layer over a cavity. This approach is consistent with simulating the cavity shear layer interaction as a rational outer solution that is associated with viscous–inviscid interaction theory. This is an extension of the concept of transpiration velocities (outer limit of inner solution for asymptotic matching) that arises in boundary-layer viscous–inviscid interactions. It leads to a self-consistent simulation of the shear layer as an inviscid vortex sheet. Also, we time average the unsteady motions of the shear layer, because these are on a timescale that is at least three orders faster than the Froude scale of the dropping body. This is a self-consistent approximation that should be realistic for the practical case of high Reynolds number of the approaching boundary layer.

Also, the flow over the separating body can be modeled using slender body theory.[6] In Refs. 4 and 5, effects of the side cavity walls were shown to be negligible in all phases of the separation process. In the analysis of this paper, the near-field flow associated with the body aerodynamics is governed by a system of nonlinear integro–differential equations. In Refs. 4 and 5, this problem was analyzed using asymptotic methods giving explicit analytical expressions for the lift force and pitching moment acting on the body in all three phases of the separation process. In the analysis, the slip-surface displacement is neglected. A more general case is when the slip surface is a free boundary supporting nonlinear boundary conditions and interacting with the solution. For the practically important case of small deflections, the boundary conditions can be linearized on the slip surface, on the length scale of the cavity. Local flow scales have larger deflections in which an iterative scheme needs to be used. The nondeflected slip surface corresponds to the initial iterate in such a small-perturbation scheme.

Problem Formulation

In this paper, we couple our previous results on the body aerodynamics with the body dynamics and analyze two-degree-of-freedom (DOF) vertical and pitching motions induced by aerodynamic and gravity forces during the separation process. The coordinate systems XYZ (attached to the cavity) and $oxyz$ (attached to the body center of gravity) are shown in Fig. 1. The oxy frame is inclined with respect to the XY frame at an angle of attack $\alpha(t)$. This frame can rotate around the oz axis with the angular speed $\omega(t) = \mathrm{d}\alpha/\mathrm{d}t$. The c.g. coordinates are expressed as $X_c = Z_c = 0$ and $Y_c(t)$; $H(X, t) = Y_c - \alpha X$ is the vertical coordinate of the body axis. Using scaling of the slender body theory,[6] we introduce the nondimensional variables

$$X = \hat{X}/\hat{l}_0, \qquad Y = \hat{Y}/\hat{a}_0, \qquad Z = \hat{Z}/\hat{a}_0, \qquad x = \hat{x}/\hat{l}_0$$

$$y = \hat{y}/\hat{a}_0, \qquad z = \hat{z}/\hat{a}_0, \qquad t = U_\infty \hat{t}/\hat{l}_0$$

$$\alpha = \hat{\alpha}/\delta, \qquad V_c = \hat{V}_c/\hat{V}_r, \qquad \omega = \delta U_\infty \hat{\omega}/\hat{l}_0 \tag{1}$$

where the body half-thickness ratio δ is treated as a small parameter. Crossflow velocities and coordinates are normalized by δU_∞ and $\hat{a}_0$, respectively. The streamwise and axial coordinates are scaled using $\hat{l}_0$, and the pressure perturbation p is normalized with respect to $\rho_\infty U_\infty^2 \delta^2 \hat{l}_0^2$.

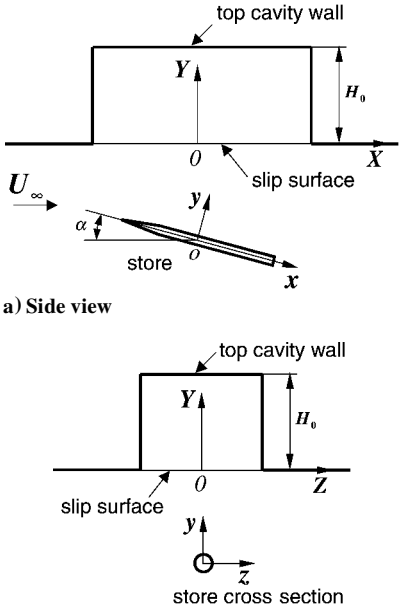

Fig. 1 Scheme of store separation.

As shown in Ref. 5, the equations for vertical and pitching body motions can be expressed in the form

$$\frac{\mathrm{d}(V_c + c_l V_a)}{\mathrm{d}t} = c_l L_1(t) - c_g, \qquad \frac{\mathrm{d}Y_c}{\mathrm{d}t} = V_c(t)$$

$$\frac{\mathrm{d}(\omega + c_m \omega_a)}{\mathrm{d}t} = c_m M_1(t), \qquad \frac{\mathrm{d}\alpha}{\mathrm{d}t} = \omega(t) \tag{2a}$$

$$V_a(t) = \int_{x_0}^{x_e} \int_0^{2\pi} \Phi(x, \theta, t) a(x)\, \mathrm{d}\theta\, \mathrm{d}x$$

$$\omega_a(t) = \int_{x_0}^{x_e} \int_0^{2\pi} \Phi(x, \theta, t) a(x) x\, \mathrm{d}\theta\, \mathrm{d}x \tag{2b}$$

$$c_g = \frac{g\hat{l}_0}{\delta U_\infty^2}, \qquad c_l = \frac{\pi \rho_\infty \hat{l}_0^3 \delta^2}{m}, \qquad c_m = \frac{\pi \rho_\infty \hat{l}_0^5 \delta^2}{I} \tag{2c}$$

where x_0 and x_e are coordinates of the body nose and base, respectively, and Φ is the near field with respect to the body (inner) flow potential. We consider the Cauchy initial-value problem for Eqs. (2a) assuming that the body speeds, c.g. coordinate, and angle of attack are prescribed at the initial time $t = 0$ as

$$V_c(0) = V_0, \qquad \omega(0) = \omega_0, \qquad Y_c(0) = Y_0, \qquad \alpha(0) = \alpha_0 \tag{2d}$$

Note that $\mathrm{d}V_a/\mathrm{d}t$ and $\mathrm{d}\omega_a/\mathrm{d}t$ in Eq. (2a) represent the time derivative of the crossflow potential (incompressible harmonic inner solution) needed for the pressure in the crossflow plane from the unsteady Bernoulli equation. The terms L_1 and M_1 are integrals involving the square of the crossflow speed that also appear in the Bernoulli law for the pressure in the crossflow inner problem. These are determined from the square of the crossflow gradient of Φ.

In this paper, analytical solutions of the problem (2a–2d) for phase 1 are obtained for small lift forces compared to the weight. Slip-surface deflections are neglected, and Eqs. (2a–2d) are transformed into two decoupled ordinary differential equations with constant coefficients. A stability analysis of their solutions is performed, and behaviors of the pitch angle $\alpha(t)$ and the vertical coordinate $Y_c(t)$ are discussed for typical cases. In addition, the theoretical model for all three phases [in Eqs. (2) (without the stability linearizations)] is evaluated by comparison of the predicted trajectories with the experimental data of Ref. 7. The paper concludes with some parametric trajectory studies.

Phase 1: Body Inside Cavity

The lift force $L(t)$ and the pitching moment $M(t)$ acting on the body moving inside the cavity are derived in Ref. 5. They are expressed as integrals along the body axis with the integrands being a power series with respect to the parameters $q_1(x,t) = 0.5a/(H_0 - H)$ and $q = 0.5a/H$, where H_0 is cavity depth shown in Figs. 1a and 1b. If the body is far from the top cavity wall and the slip surface, then q_1 and q can be treated as small parameters. When terms of the order of $\mathcal{O}(q^3, q_1^3)$ are neglected, the body cross section vertical velocity $V_a^+(t)$ and angular velocity $\omega_a^+(t)$ are expressed in the form

$$V_a^+(t) \equiv \alpha_{11}(t)V_c(t) - \alpha_{12}(t)\omega(t)$$

$$\omega_a(t) \equiv \alpha_{12}(t)V_c(t) - \alpha_{22}(t)\omega(t) \tag{3a}$$

$$\alpha_{11}(t) \equiv \pi[g_0 + G_0(t)], \qquad \alpha_{12}(t) = \pi[g_1 + G_1(t)]$$

$$\alpha_{22}(t) \equiv \pi[g_2 + G_2(t)] \tag{3b}$$

$$g_0 \equiv \int_{x_0}^{x_e} a^2(x)\,\mathrm{d}x, \qquad g_1 \equiv \int_{x_0}^{x_e} a^2(x)x\,\mathrm{d}x$$

$$g_2 \equiv \int_{x_0}^{x_e} a^2(x)x^2\,\mathrm{d}x \tag{3c}$$

$$G_0(t) \equiv 2\int_{x_0}^{x_e} \left[q_1^2(x,t) - q^2(x,t)\right]a^2(x)\,\mathrm{d}x \tag{3d}$$

$$G_1(t) \equiv 2\int_{x_0}^{x_e} \left[q_1^2(x,t) - q^2(x,t)\right]a^2(x)x\,\mathrm{d}x$$

$$G_2(t) \equiv 2\int_{x_0}^{x_e} \left[q_1^2(x,t) - q^2(x,t)\right]a^2(x)x^2\,\mathrm{d}x \tag{3e}$$

This transformation helps to express the dynamic equations in a form convenient for further discussion of the body trajectory features. When Eqs. (3a–3e) are used, the trajectory equations (2a) can be integrated once and expressed in the form

$$\frac{\mathrm{d}Y_c}{\mathrm{d}t} = -\frac{b_{22}(t)}{\Delta(t)}c_g t + \frac{\Delta_1(t)}{\Delta(t)}V_0 + c_l\pi\omega_0 b_1(t) \tag{4a}$$

$$\frac{\mathrm{d}\alpha}{\mathrm{d}t} = \frac{b_{21}(t)}{\Delta(t)}c_g t + \frac{\Delta_2(t)}{\Delta(t)}\omega_0 + c_m\pi V_0 b_2(t) \tag{4b}$$

where the coefficients are defined as

$$b_{11}(t) \equiv 1 + c_l\alpha_{11}(t), \qquad b_{12}(t) \equiv c_l\alpha_{12}(t)$$

$$b_{21}(t) \equiv c_m\alpha_{12}(t), \qquad b_{22}(t) \equiv 1 - c_m\alpha_{22}(t)$$

$$\Delta \equiv b_{11}(t)b_{22}(t) + b_{12}(t)b_{21}(t)$$

$$\Delta_1 \equiv b_{11}(0)b_{22}(t) + b_{12}(t)b_{21}(0)$$

$$\Delta_2 \equiv b_{11}(t)b_{22}(0) + b_{12}(0)b_{21}(t)$$

$$b_1 \equiv (1/\Delta)\{(1 - c_m\pi g_2)[G_1(t) - G_1(0)] + c_m\pi g_1[G_2(t) - G_2(0)]$$
$$+ c_m\pi[G_1(0)G_2(t) - G_1(t)G_2(0)]\}$$

$$b_2 \equiv (1/\Delta)\{(1 + c_l\pi g_0)[G_1(0) - G_1(t)] + c_l\pi g_1[G_0(t) - G_0(0)]$$
$$+ c_l\pi[G_1(0)G_0(t) - G_1(t)G_0(0)]\}$$

The first term of Eqs. (4a–4b) models the gravity effect, the second term comes from the initial conditions, and the third term arises from the boundary and initial conditions. The angular acceleration is proportional to the product of the pitching moment coefficient c_m, the gravity force coefficient c_g, and the value $g_1 + G_1(t)$ characterizing the displacement of the center of pressure from the c.g.[8] Equations (4) can be solved numerically using, for example, the Runge–Kutta method. Note that the slip-surface effect and the top-wall effect rapidly decrease as the body moves away from these boundaries. Neglecting terms of the order of $\mathcal{O}(q^2 + q_1^2)$, which are associated with the boundary effects, the solution of Eqs. (4) can be expressed in explicit analytical form:

$$Y_c(t) = Y_0 + V_0 t - \frac{1 - \pi c_m g_2}{2\Delta_0}c_g t^2$$

$$\alpha(t) = \alpha_0 + \omega_0 t + \frac{\pi g_1 c_m c_g}{2\Delta_0}t^2 \tag{5a}$$

$$\Delta_0 = (1 + c_l\pi g_0)(1 - c_m\pi g_2) + c_l c_m \pi^2 g_1^2 \tag{5b}$$

Equations (5) show that the c.g. coordinate $Y_c(t)$ and the pitch angle $\alpha(t)$ are parabolic functions of time when the body moves in an unbounded fluid at rest.

It is also possible to obtain analytical solutions of Eqs. (4), when the lift and moment are small compared to the body weight. This is typical for many practical cases because the coefficients c_l and c_m are proportional to the air density to body density ratio, $\rho_\infty/\rho_b \ll 1$. For a body of uniform density, nondimensional ballistic parameters may be defined as

$$c_l = \frac{\rho_\infty}{\rho_b\pi g_0}, \qquad c_m = \frac{\rho_\infty}{\rho_b\pi g_2}, \qquad \frac{c_l}{c_m} = \frac{g_2}{g_0} \tag{6}$$

For the experimental conditions,[7] the coefficients c_l and c_m as well as other basic parameters are shown in Tables 1 and 2, where the gravity force coefficient is calculated at the freestream speed $U_\infty = 77.1$ m/s.

If terms linear in c_l and c_m are retained in Eqs. (4), the approximate linear and angular trajectories are

$$Y_c = Y_0 + V_0 t - 0.5(1 - \pi c_l g_0)c_g t^2$$

$$\alpha = \alpha_0 + \omega_0 t + 0.5\pi g_1 c_m c_g t^2 \tag{7}$$

The c.g. coordinate and the pitch angle are parabolic functions of time. In the first-order approximation, the vertical motion corresponds to a pure gravity drop. The lift force gives a small negative correction of the c.g. acceleration similar to the case of a plunging cylinder in the presence of a shear layer considered in Ref. 4. As will be shown, the analytical expressions (7) are consistent with trends of numerical solutions and experimental data.

Table 1 Nondimensional parameters of models[7]

Model	δ	X_e	g_0	g_1	g_2
B1N1	0.31250E−01	0.51333E+00	0.86206E+00	0.68807E−01	0.66707E−01
B4N2	0.31250E−01	0.49500E+00	0.86206E+00	0.53002E−01	0.57596E−01
B5N5	0.32609E−01	0.62261E+00	0.85606E+00	0.16423E+00	0.12753E+00

Table 2 Aerodynamic and gravity acceleration coefficients for models[7]

Model	c_l	c_m	$c_g U_\infty^2$, m^2/s^2	c_g
B1N1	0.29915E−03	0.22204E−02	0.95585E+02	0.16080E−01
B4N2	0.72519E−03	0.38857E−02	0.95585E+02	0.16080E−01
B5N5	0.36773E−02	0.24684E−01	0.87786E+02	0.14768E−01

Phase 3: Body Outside Cavity

If the body is totally outside the cavity and moves into an external freestream, the lift force and pitching moment are again expressed as integrals along the body axis with the integrands being a power series with respect to the parameter $q = 0.5a/H$ (see Ref. 5). When these analytical solutions are analyzed, the slip-surface effect on the body trajectory is found to be proportional to the quantity

$$\int_{x_0}^{x_e} qa^2 a_x \,\mathrm{d}x + \int_{x_0}^{x_e} q^2 a^2 \,\mathrm{d}x \sim \frac{\bar{q}}{3} + \overline{q^2} g_0 + \mathcal{O}(\overline{q^3} g_0) \tag{8}$$

where the over bars denote averaging along the body axis. For typical cases, the body shape factor is given by Eq. (3c), $g_0 = \mathcal{O}(1)$. The average distance parameter is $\bar{q} \le 0.5$. Its maximum value $\bar{q} = 0.5$ corresponds to contact of the body surface with the slip surface. The maximum values of the first and second terms in Eq. (8) are $\frac{1}{6}$ and $\frac{1}{4}$, respectively. As the body drops, both terms decrease quickly, and the slip-surface effect vanishes. Thus, dominant terms are associated with the body drop in an unbounded uniform stream. In this case, the equations for the lift force and pitch moment can be reduced to

$$L = \pi\left[-g_0 \frac{\mathrm{d}V_c}{\mathrm{d}t} + g_1 \frac{\mathrm{d}\omega}{\mathrm{d}t} - (V_c - \alpha)a_e^2 + \omega\left(g_0 + x_e a_e^2\right)\right] \tag{9a}$$

$$M = \pi\left[-g_1 \frac{\mathrm{d}V_c}{\mathrm{d}t} + g_2 \frac{\mathrm{d}\omega}{\mathrm{d}t} + (V_c - \alpha)\left(g_0 - x_e a_e^2\right) + \omega x_e^2 a_e^2\right] \tag{9b}$$

where $a_e = a(x_e)$ is the base radius ($a_e = 1$ for a cylindrical afterbody). These expressions were derived for bodies with a sharp nose, $a(x_0) = 0$. Substitution of Eqs. (9a) and (9b) into the trajectory equations (2a) and integration once give the linear ordinary differential equation (ODE) system (with constant coefficients)

$$\frac{\mathrm{d}V_c}{\mathrm{d}t} = c_{11}(V_c - \alpha) + c_{12}\omega - c_{10}$$

$$\frac{\mathrm{d}\omega}{\mathrm{d}t} = c_{21}(V_c - \alpha) + c_{22}\omega + c_{20} \tag{10a}$$

$$c_{10} = \frac{1 - c_m \pi g_2}{\Delta_0} c_g, \qquad c_{20} = \frac{c_m c_g \pi g_1}{\Delta_0}$$

$$c_{11} = \frac{c_l \pi}{\Delta_0}\left[c_m \pi g_1\left(g_0 - x_e a_e^2\right) - (1 - c_m \pi g_2)a_e^2\right] \tag{10b}$$

$$c_{12} = \frac{c_l \pi}{\Delta_0}\left[(1 - c_m \pi g_2)\left(g_0 + x_e a_e^2\right) + c_m \pi g_1 x_e^2 a_e^2\right] \tag{10c}$$

$$c_{21} = \frac{c_m \pi}{\Delta_0}\left[(1 + c_l \pi g_0)\left(g_0 - x_e a_e^2\right) + c_l \pi g_1 a_e^2\right] \tag{10d}$$

$$c_{22} = \frac{c_m \pi}{\Delta_0}\left[(1 + c_l \pi g_0)x_e^2 a_e^2 - c_l \pi g_1\left(g_0 + x_e a_e^2\right)\right] \tag{10e}$$

where Δ_0 is given by Eq. (5b).

We consider the Cauchy problem for Eqs. (10a) assuming that the body is totally outside the cavity for $t \ge t_0$, and its initial speeds, coordinate, and pitch angle are

$$V_c(t_0) = V_0', \qquad \omega(t_0) = \omega_0', \qquad Y_c(t_0) = Y_0', \qquad \alpha(t_0) = \alpha_0' \tag{11}$$

From Eqs. (10a), the angular velocity ω and the function $W(t) = V_c(t) - \alpha(t)$ are solutions of the decoupled equations

$$\frac{\mathrm{d}^2 W}{\mathrm{d}t^2} - 2\gamma \frac{\mathrm{d}W}{\mathrm{d}t} + \kappa W + c_1 = 0, \qquad \frac{\mathrm{d}^2 \omega}{\mathrm{d}t^2} - 2\gamma \frac{\mathrm{d}\omega}{\mathrm{d}t} + \kappa \omega + c_2 = 0 \tag{12}$$

where the constant coefficients are

$$\gamma = \frac{c_m \pi a_e^2}{2\Delta_0}\left[x_e^2 - \frac{c_l}{c_m} + \pi c_l\left(x_e^2 g_0 - 2x_e g_1 + g_2\right)\right]$$

$$\kappa = \frac{c_m \pi}{\Delta_0}\left[g_0 - a_e^2 x_e - c_l \pi a_e^2 (g_0 x_e - g_1)\right] \tag{13a}$$

$$c_1 = \frac{c_m c_g \pi}{\Delta_0}\left(g_1 - x_e^2 a_e^2\right), \qquad c_2 = \frac{c_m c_g \pi}{\Delta_0}\left(g_0 - x_e a_e^2\right) \tag{13b}$$

The characteristic (secular) equation for the eigenvalues of ODE system (10a) and its solutions are

$$\lambda^2 - 2\gamma\lambda + \kappa = 0, \qquad \lambda_1 = \gamma + i\Omega$$

$$\lambda_2 = \gamma - i\Omega, \qquad \Omega = \sqrt{\kappa - \gamma^2} \tag{14}$$

Various cases significant for the trajectory stability will now be discussed.

Eigenvalues λ_1 and λ_2 Are Complex

If λ_1 and λ_2 are complex, then the trajectory parameters are expressed in the form

$$V_c(t) = V_0' + (d - c_2\tau)/\kappa + e^{\gamma\tau}(A_1 \cos\Omega\tau + A_2 \sin\Omega\tau)$$

$$\omega = -(c_2/\kappa) + e^{\gamma\tau}(B_1 \cos\Omega\tau + B_2 \sin\Omega\tau) \tag{15a}$$

$$Y_c(t) = Y_0' + (V_0' + d/\kappa)\tau - (c_2/2\kappa)\tau^2 + (e^{t\gamma}/\kappa) \times [(\gamma A_1 - \Omega A_2)\cos\Omega\tau + (\Omega A_1 + \gamma A_2)\sin\Omega\tau] \tag{15b}$$

$$\alpha(t) = \alpha_0' - (1/\kappa)\left\{c_2\tau + \gamma B_1 - \Omega B_2 - e^{\gamma\tau}[(\gamma B_1 - \Omega B_2)\cos\Omega\tau + (\Omega B_1 + \gamma B_2)\sin\Omega\tau]\right\} \tag{15c}$$

where $\tau = t - t_0$ and $d = -\kappa(V_0' - \alpha_0') - c_1 - \gamma B_1 + \Omega B_2$. The coefficients A_1, A_2, B_1, and B_2 are determined from the initial conditions (11) and Eqs. (10a). They are expressed as

$$A_1 = -\frac{d}{\kappa}, \qquad A_2 = \frac{c_2}{\Omega\kappa} + \frac{\dot{V}_0 - \gamma A_1}{\Omega}$$

$$\dot{V}_0 = \frac{\mathrm{d}V(0)}{\mathrm{d}t} = c_{11}(V_0' - \alpha_0') + c_{12}\omega_0' - c_{10} \tag{16a}$$

$$B_1 = \omega_0' + \frac{c_2}{\kappa}, \qquad B_2 = \frac{\dot{\omega}_0 - \gamma B_1}{\Omega}$$

$$\dot{\omega}_0 = \frac{\mathrm{d}\omega(0)}{\mathrm{d}t} = c_{21}(V_0' - \alpha_0') + c_{22}\omega_0' + c_{20} \tag{16b}$$

Equations (15) indicate that the body motion includes two components. The first terms of Eqs. (15a) and (15b) correspond to body rotation with the constant angular speed $-c_2/\kappa$ and a vertical translation with uniform acceleration $-c_2/\kappa$. Also present is a drift with constant velocity $\alpha_0' - (c_1 + 2\gamma B_1 - \dot{\omega}_0)/\kappa$ that depends on the initial angle of attack and angular velocity. These terms are associated with a nonoscillatory motion, which is called the mean state. The second component corresponds to periodic modulations of the mean state. These oscillations are neutral for $\gamma = 0$, unstable for positive γ, and stable for negative γ. For zero base radius $a_e = 0$, Eq. (13) specializes to

$$\gamma = 0, \qquad \kappa = \Omega^2 = (c_m \pi/\Delta_0)g_0, \qquad c_1 = (c_m c_g \pi/\Delta_0)g_1$$

$$c_2 = (c_m c_g \pi/\Delta_0)g_0$$

This case corresponds to neutral oscillations. For heavy bodies with base radius $a_e = 1$ and small ballistic coefficients $c_l \ll 1$ and $c_m \ll 1$, we can linearize about c_l and c_m. Equations (13) yield

$$\gamma = \pi c_m\left(x_e^2 - c_l/c_m\right), \qquad \kappa = \Omega^2 = c_m \pi(g_0 - x_e) \tag{17a}$$

$$c_1 = \pi c_m c_g\left(g_1 - x_e^2\right), \qquad c_2 = \pi c_m c_g(g_0 - x_e)$$

$$d = \pi c_l(\omega_0 + c_g) \tag{17b}$$

Equations (17) show that oscillations are unstable for $x_e^2 > c_l/c_m$. This case fits the experimental conditions of Ref. 7. For $x_e^2 \le c_l/c_m$, oscillations are stable or neutral. In all cases the increment is small, $\gamma \sim c_m \sim \Omega^2 \ll 1$. The expressions for the vertical speed and angular velocity are

$$V_c = V_0' - c_g\tau + A_1(e^{\gamma\tau}\cos\Omega\tau - 1) + A_2 e^{\gamma\tau}\sin\Omega\tau$$

$$\omega = -c_g + e^{\gamma\tau}(B_1\cos\Omega\tau + B_2\sin\Omega\tau)$$

The first equation indicates that the c.g. oscillates near its mean state associated with free drop. If the body dynamics is stable, $\gamma < 0$, then the oscillations vanish as $\tau \to \infty$. Nevertheless, they induce the constant vertical velocity $-A_1 = c_l\pi(\omega_0' + c_g)/\Omega^2$. The second equation shows that the angular velocity oscillates near its mean level, $\bar{\omega} = -c_g$, associated with free drop.

Eigenvalues λ_1 and λ_2 Are Real

If $\lambda_1 = \gamma + \nu$ and $\lambda_2 = \gamma - \nu$ [$\nu = \sqrt{(\gamma^2 - \kappa)}$] are real, then the solution of Eqs. (10a) or Eqs. (12) is

$$V_c(t) = V_0' + (d - c_2\tau)/\kappa + e^{\gamma\tau}(A_1 ch\nu\tau + A_2 sh\nu\tau)$$

$$\omega = -(c_2/\kappa) + e^{\gamma\tau}(B_1 ch\nu\tau + B_2 sh\nu\tau) \tag{18a}$$

$$Y_c(t) = Y_0' + (V_0' + d/\kappa)\tau - (c_2/2\kappa)\tau^2 + (e^{t\gamma}/\kappa)[(\gamma A_1 - \nu A_2)ch\nu\tau + (\gamma A_2 - \nu A_1)sh\nu\tau] \tag{18b}$$

$$\alpha(t) = \alpha_0' - (1/\kappa)\{c_2\tau + \gamma B_1 - \nu B_2 - e^{\gamma\tau}[(\gamma B_1 - \nu B_2)ch\nu\tau + (\gamma B_2 - \nu B_1)sh\nu\tau]\} \tag{18c}$$

where $d = -\kappa(V_0' - \alpha_0') - c_1 - \gamma B_1 + \nu B_2$ and the coefficients are

$$A_1 = -(d/\kappa), \qquad A_2 = c_2/\nu\kappa + (\dot{V}_0 - \gamma A_1)/\nu$$

$$B_1 = \omega_0' + c_2/\kappa, \qquad B_2 = (\dot{\omega}_0 - \gamma B_1)/\nu \tag{19}$$

Again the body motion has two components. The first component is similar to that of the earlier case. It is associated with a pure gravity drop and can be treated as a basic state. The second component is relevant to an exponential drift from or toward the basic state depending on the signs of the eigenvalues. If $\lambda_1 < 0$ and $\lambda_2 < 0$, then the exponents decay as $\tau \to \infty$, and the body motion evolves from the initial conditions to the basic state, which includes rotation with constant angular velocity and translation with constant acceleration. If λ_1 and/or λ_2 are positive, then the exponential terms grow with time, and the body departs from its basic state (aperiodic divergence). If $\nu = 0$, then the second component of the body motion is governed by the sign of γ.

The aforementioned analytical solutions and stability characteristics of the body dynamics can be used for fast qualitative estimations of the body trajectory outside the cavity. To our knowledge, these results are new.

Results and Discussion

To calculate the body trajectory including all phases of the separation process Eqs. (2a) are numerically integrated using a sixth-order Runge–Kutta scheme (see Ref. 9). Our computational code includes a module that calculates the lift force and pitching moment for phases 1–3 using the analytical results of Ref. 5. The accuracy of the predictions can be related to the size of the perturbation parameters and uncertainties in the experimental launch conditions. (Because these data are referenced, their accuracy can be obtained from the authors.) In the best cases, the accuracy can be as good as a few percent when the aerodynamic forces are small compared to the weight and the characteristic pitch inertia with experimental initial conditions that matched those assumed in the theory. Large excursions can result if large-scale shear layer motions occur and other disturbances evolve in the external flow.

The combined asymptotic and numerical method described provides a means to calculate rapidly body trajectories. One trajectory is normally predicted in less than 0.5 min using a personal computer Pentium 166. This quick-turnaround personal-computer-oriented tool will be compared to the subsonic experimental data[7] in what follows.

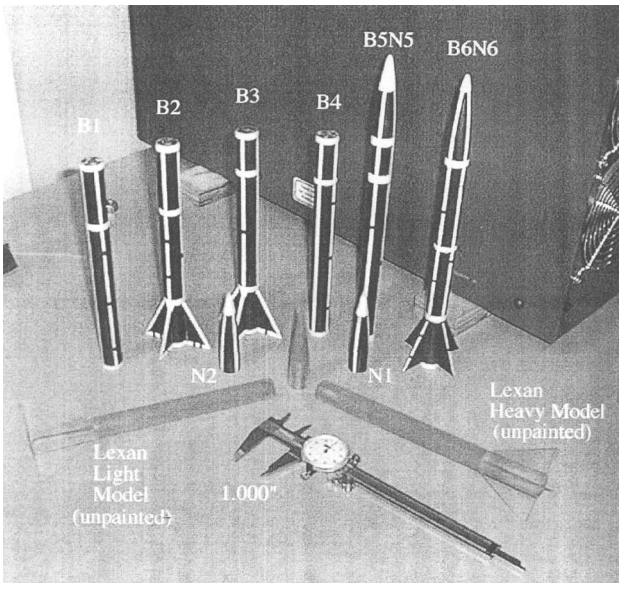

Fig. 2 Models for free-drop tests in the IIT wind tunnel.

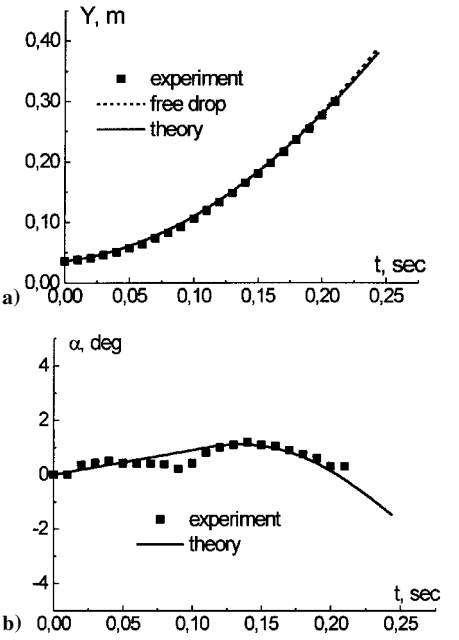

Fig. 3 Model B4N2, U_∞ = 62.3 m/s, Y_0 = 1.42 in. (0.0361 m), α_0 = 0 deg, V_0 = 8 in./s (0.2032 m/s), and ω_0 = 9 deg/s.

Experimental Data

Drop tests[7] were conducted in the National Diagnostic Wind Tunnel of the Illinois Institute of Technology (IIT) Fluid Dynamics Research Center at the Mach number range $0.12 < M < 0.23$. The rectangular cavity of 20 in. (0.508 m) length, 41 in. (1.0414 m) width, and 4 in. (0.1016 m) height was mounted on the top wall of the wind-tunnel test section. The test articles were bodies of revolution of radius $\hat{a}_0 = \frac{3}{8}$ in. (0.009525 m) and nose length $\hat{x}_n = 3.56$ in. (0.090424 m) (Fig. 2). Two models (B1N1 and B4N2) were ogive cylinders 12 in. (0.3048 m) length. The third model (B5N5) had an elliptic nose and a total length of 11.5 in. (0.2921 m). The heaviest model, B1N1, had mass $m = 111.85$ g, moment of inertia $I = 0.0014\ \text{kg}\cdot\text{m}^2$, and c.g. location $\hat{x}_0 = 6.16$ in. (0.1565 m). For model B4N2, $m = 46.14$ g, $I = 0.0008\ \text{kg}\cdot\text{m}^2$, and $\hat{x}_0 = 5.94$ in. (0.1509 m). The lightest model, B5N5, had $m = 8.72$ g and $I = 0.000015\ \text{kg}\cdot\text{m}^2$. In these experiments, bodies were dropped from a cavity in the IIT wind tunnel.

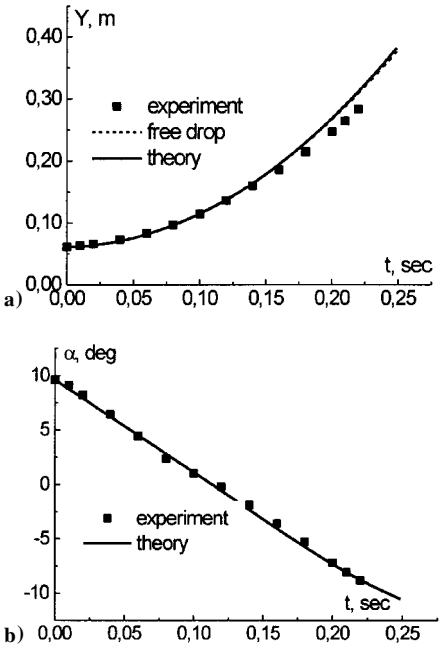

Fig. 4 Model B4N2, U_∞ = 41.3 m/s, Y_0 = 2.4 in. (0.061 m), α_0 = 9.6 deg, V_0 = 2 in./s (0.0508 m/s), and ω_0 = − 80 deg/s.

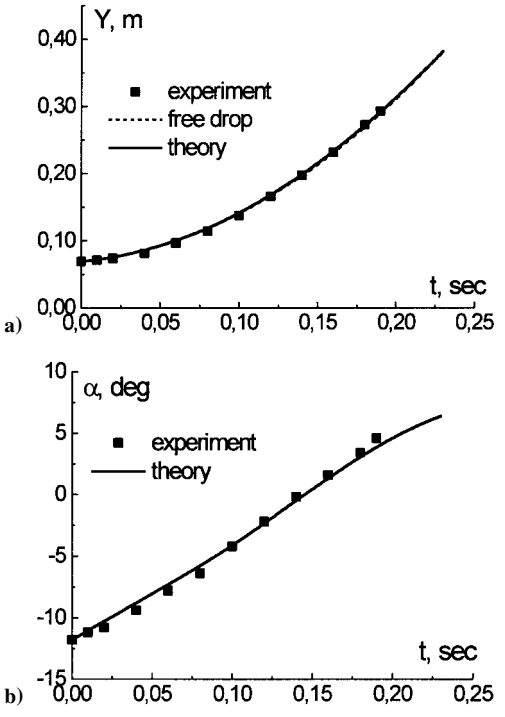

Fig. 5 Model B1N1, U_∞ = 62.7 m/s, Y_0 = 2.72 in./s (0.0691 m), α_0 = − 11.8 deg, V_0 = 9 in./s (0.2286 m/s), and ω_0 = 75 deg/s.

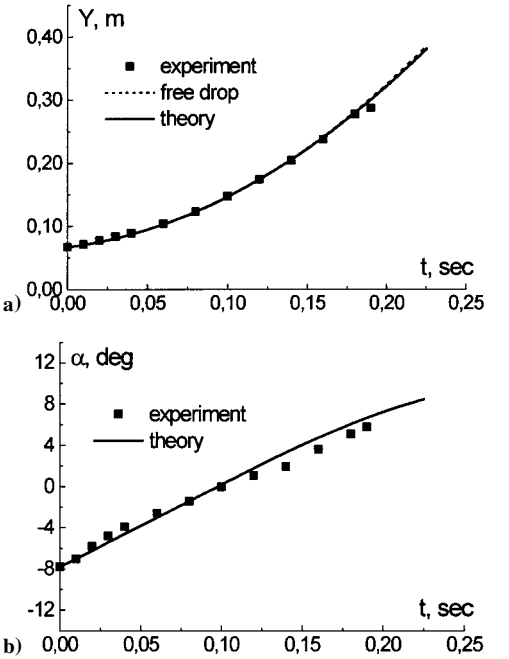

Fig. 6 Model B1N1, U_∞ = 40.8 m/s, Y_0 = 2.65 in. (0.0673 m), α_0 = − 7.8 deg, V_0 = 15 in./s (0.381 m/s), and ω_0 = 80 deg/s.

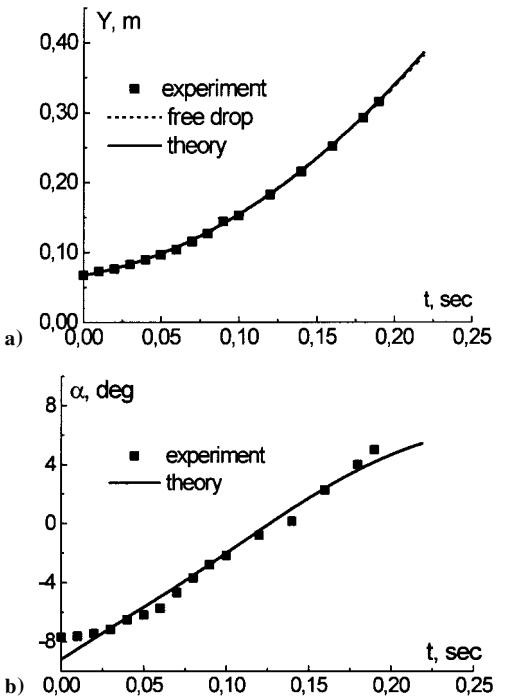

Fig. 7 Model B4N2, U_∞ = 40.6 m/s, Y_0 = 2.65 in. (0.0673 m), α_0 = − 9.2 deg, V_0 = 15 in./s (0.381 m/s), and ω_0 = 70.8 deg/s.

The models were released by withdrawing pins holding them at their noses and tails.

Comparison with Experiment

Preliminary analysis of the experimental data shows that during the release time $t_r \approx 0.03$ s, the initial angular and vertical velocities can be essentially affected by uncontrolled disturbances that may be induced by the release mechanism. During the release time, the gravity force may increase the pitch rate, if the model ends are not released simultaneously. This motivated identification of the actual initial angular speed $\hat{\omega}_0$ and vertical velocity $\hat{V}_0$ by differentiating the experimental distributions of the pitch angle $\hat{\alpha}(\hat{t})$ and the c.g. vertical coordinate $\hat{Y}_c(\hat{t})$.

Figures 3a–10a show comparisons between predicted (solid lines) and experimental (symbols) c.g. trajectories for all three models. Dashed lines indicate the free-drop trajectories under the gravity force only. As already noted, the lift is small compared to the body weight. The free drop in a vacuum is very close to the computational results and the experimental data for moderate angles of attack, especially for the heavier model, B1N1. However, the vacuum curve diverges from the experimental data if the body enters into the external stream at relatively large $\hat{\alpha}$. This is clearly seen in Figs. 4a, 8a, and 10a. In these cases, the theoretical prediction accounting for aerodynamic loads is in a good agreement with the experiment. Moreover, the theoretical model is capable of capturing trajectory nuances shown in Fig. 8a.

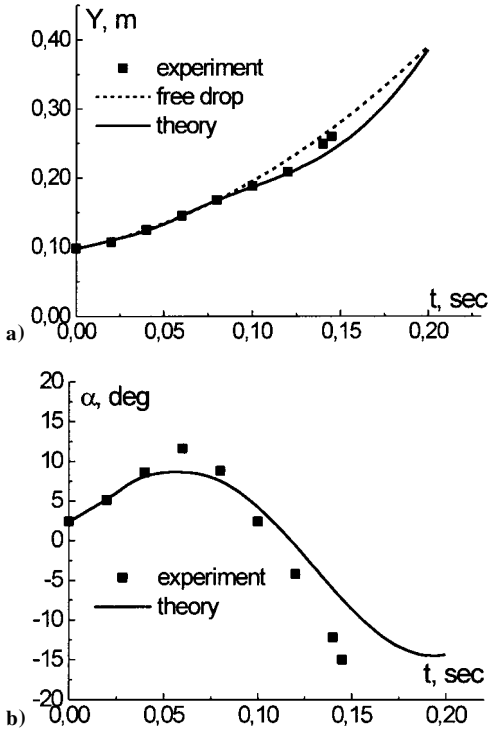

Fig. 8 Model B5N5, U_∞ = 62.5 m/s, Y_0 = 3.85 in. (0.978 m), α_0 = 2.4 deg, V_0 = 19 in./s (0.4826 m/s), and ω_0 = 140 deg/s.

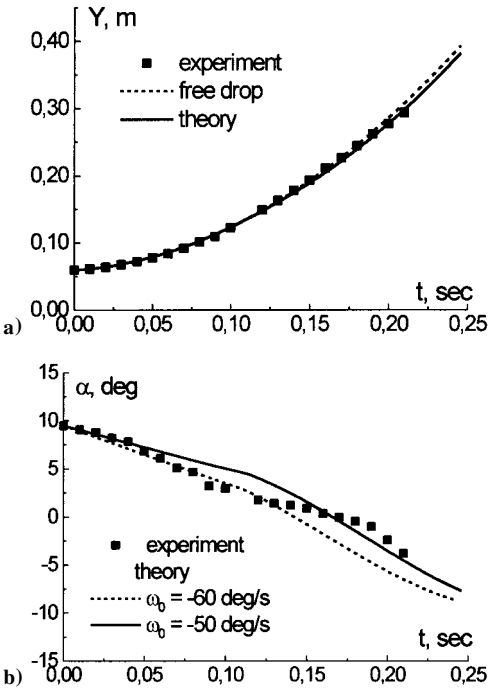

Fig. 9 Model B4N2, U_∞ = 62.3 m/s, Y_0 = 2.33 in. (0.592 m), α_0 = 9.5 deg, and V_0 = 6 in./s (0.1524 m/s).

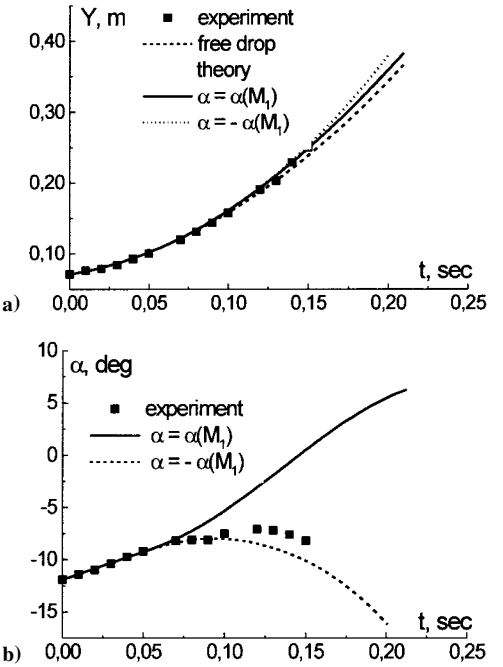

Fig. 10 Model B4N2, U_∞ = 62.1 m/s, Y_0 = 2.8 in. (0.0711 m), α_0 = − 11.9 deg, V_0 = 15 in./s (0.381 m/s), and ω_0 = 52.86 deg/s.

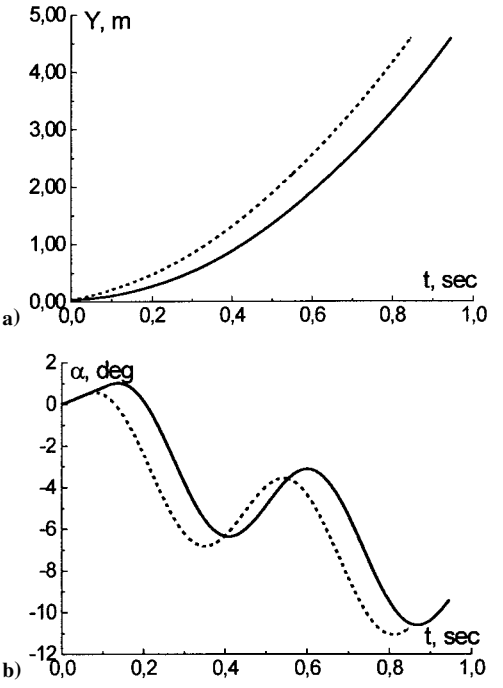

Fig. 11 Effects of initial vertical velocity: model B4N2, U_∞ = 62.3 m/s; Y_0 = 1.42 in. (0.0361 m); α_0 = 0 deg; ω_0 = 8 deg/s; ——, V_0 = 8 in./s (0.2032 m/s); – – –, V_0 = 50 in./s (1.27 m/s).

Figures 3b–10b show a comparison between predicted (lines) and experimental (symbols) histories of the angle of attack $\hat{\alpha}(t)$. Figures 3b–6b show good agreement between the theory and the experiment. The agreement is only satisfactory for the cases shown in Figs. 7b–9b. Rough estimates indicate that the initial growth of $\hat{\alpha}$ (Fig. 7b) may be associated with an initial pitch impulse generated by the release mechanism under a gravitational couple from the pins. In this case, both the initial angle of attack and angular speed were estimated from the experimental data. These were used as the initial conditions for the calculations. For the lightest model, B5N5 (Fig. 8b), the discrepancy seems to be due to the difference between the actual nose shape (elliptic) and the shape used in our calculations (parabolic ogive). Unfortunately, calculations were not possible for the actual nose because its geometry was not available. Note that the nose shape becomes more important at large pitch angles. The divergence of the predicted and experimental curves in Fig. 9b seems to be due to the flow inside the cavity, which is presently not included in our modeling. Namely, the nonuniform upwash field due to the recirculatory flow in the cavity has not been included. Such an upwash field will change the crossflow angle of attack from that due solely to the vertical speed of the body, which has been accounted for in the approximate model described here. This can be thought of as a first estimate of the flow physics. The effect of the upwash field can be considered a refinement of this

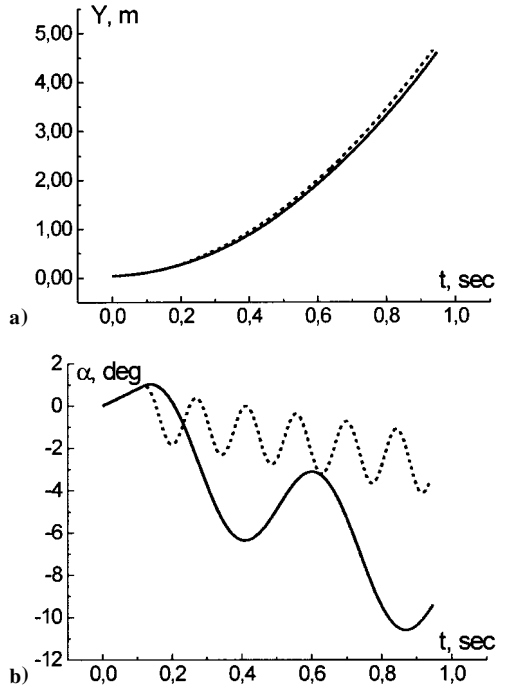

Fig. 12 Effect of freestream velocity on the body trajectory: model B4N2, Y_0 = 1.42 in. (0.0361 m); α_0 = 0 deg; V_0 = 8 in./s; ω_0 = 8 deg/s; ——, U_∞ = 62.3 m/s; – – –, U_∞ = 200 m/s.

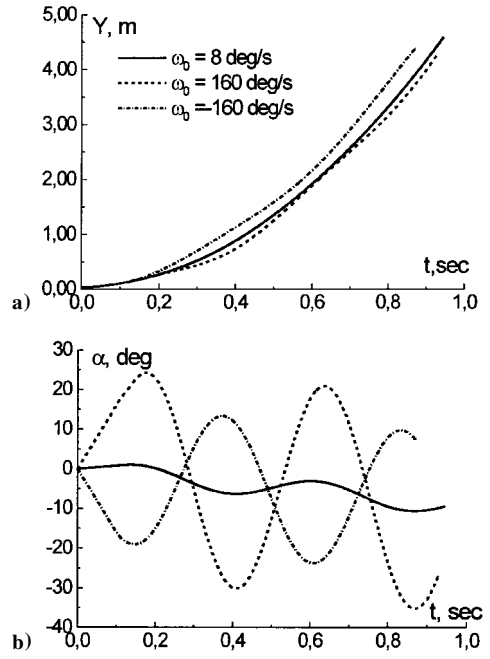

Fig. 13 Influence of the initial angular speed on the body trajectory: model B4N2, U_∞ = 62.3 m/s, Y_0 = 1.42 in. (0.0361 m), α_0 = 0 deg, and V_0 = 8 in./s (0.2032 m/s).

model in which this recirculatory flow can be estimated from the empty cavity flow. An inviscid approximation for the latter is given in Ref. 4 for deep cavities. (Deep cavities are almost bridged at their top end by the shear layer in contrast to shallow cavities for which the shear layer will collide with their bottom.) Further refinements would include the interaction of the moving body with this nonuniform flow for both deep and shallow cavities. Pitch oscillations observed in phase 1 (body is totally inside the cavity) clearly indicate the presence of this effect, which may also explain the substantial difference between the theory and the experiment shown in Fig. 10b.

As indicated earlier, the pitch behavior in phase 3 (body is outside the cavity) strongly depends on the entry condition, which is a

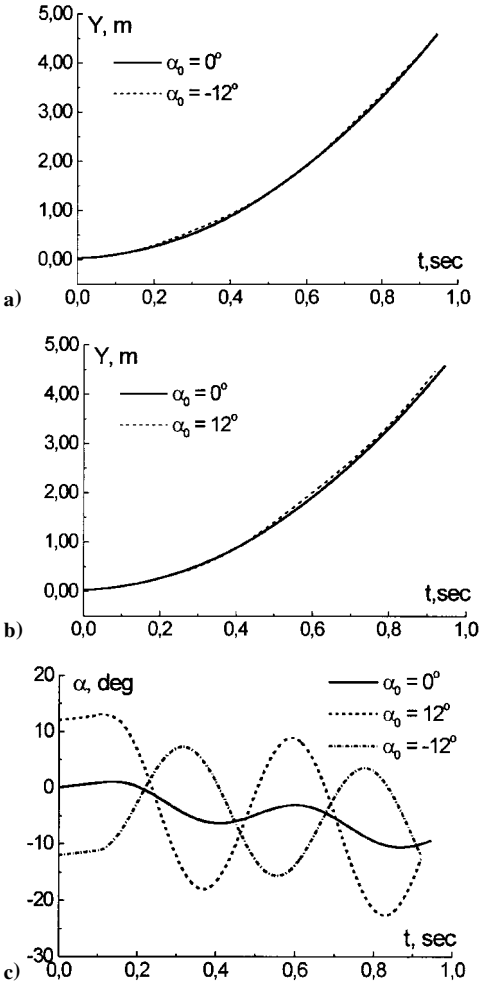

Fig. 14 Influence of the initial pitch angle on the body trajectory: model B4N2, U_∞ = 62.3 m/s, Y_0 = 1.42 in. (0.0361 m), V_0 = 8 in./s (0.2032 m/s), and ω_0 = 8 deg/s.

function of the angular velocity, vertical speed, and their derivatives. For the case shown in Fig. 10b, the shear layer displacement from its basic state into the cavity may cause a phase jump of the right-hand-side term in Eq. (2a) from 0 to 180 deg. Such a jump affects the pitch history outside the cavity. This is illustrated in Fig. 10b by the dotted line that was calculated with the opposite sign of the pitching moment. It is seen that this curve is in a good agreement with the experimental data. On the other hand, experimental curves, shown in Figs. 5b, 6b, and 7b for approximately the same initial conditions, have a regular behavior, that is, they are in a good agreement with the computations performed without changes of the sign of pitching moment. These findings suggest that there is a bifurcation in the pitch history $\alpha(t)$ when the body enters into the external stream. The trajectory equations allow such a bifurcation because the aerodynamic forcing terms of Eqs. (2a) are nonlinear (quadratic) functions of speeds V and ω. One of two possible trajectories is selected when the body crosses the shear layer. Therefore, phase 2 serves as a trigger of the pitch bifurcation. Accurate modeling of this mechanism is important for prediction of the pitch history and store trajectory in the next phase, when the store is outside the cavity. To verify this hypothesis additional theoretical, numerical, and experimental studies are needed.

Parametric Studies

Parametric studies of the body trajectory were conducted for different initial conditions, body parameters, and freestream speeds. The results are shown in Figs. 11–15. Variations of the initial vertical velocity cause not only c.g. acceleration but phase shift of the pitch angle (Fig. 11). In accord with the analytical solution discussed earlier, an increase of the freestream velocity leads to a substantial increase of the mean pitching angle and the pitch oscillation

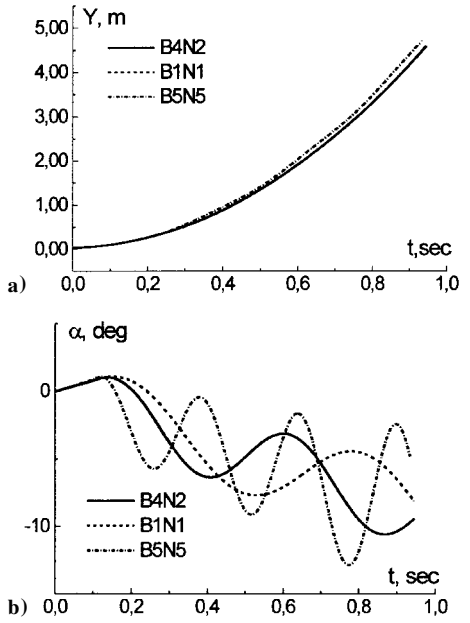

Fig. 15 Trajectories of different models: U_∞ = 62.3 m/s, Y_0 = 1.42 in. (0.0361 m), α_0 = 0 deg, V_0 = 8 in./s (0.2032 m/s), and ω_0 = 8 deg/s.

frequency (Fig. 12), while the c.g. trajectory is changed slightly. Figure 13 shows that the pitch oscillation amplitude increases and the phase shift occurs as the initial angular speed increases. Amplification of the pitch oscillations is stronger in the case of positive ω_0 with the c.g. trajectory also noticeably affected. The effect of the initial pitch angle is similar to the effect of ω_0 (compare Figs. 14 and 15). However, the variation of the c.g. trajectory in this case is smaller.

Trajectory dependencies on the body shape are shown in Fig. 15. The calculations were performed for three experimental models of Ref. 7 under the same initial conditions. As expected, the highest amplitude and frequency of the body oscillations correspond to the lightest model, B5N5. It is also seen that the body trajectories outside the cavity are consistent with the analytical solution discussed earlier.

Conclusions

This paper discussed modeling of two-DOF vertical and pitching motions of thin bodies of revolution separating from a rectangular cavity into an external freestream. The problem is analyzed using combined asymptotic and numerical methods. The body dynamic equations include aerodynamic forces and moments, which are predicted using approximate analytical solutions obtained in our previous studies within the framework of the slender body theory. Different phases of the separation process were analyzed using small perturbation theories. This leads to simplifications of the trajectory equations and their integration in closed form for different typical cases associated with phase 1 (body is inside the cavity) and phase 3 (body is outside the cavity). These analytical solutions provide explicit dependencies of the body trajectory on the flow and body characteristics, which allows identification of the critical parameters and insight gained into the physics of the separation process.

The numerical code predicting the trajectories for all three phases of store separation was validated by comparison with the experiment. For a major portion of the data, the calculations are in a good agreement with experiment. Moreover, the theory is able to capture nuances of the body pitching observed experimentally. These results confirm our theoretical model. However, there are cases when the agreement is only satisfactory. The body separation is affected by more complex flow phenomena, which are not captured by our model. One discrepancy seems to be due to the slip-surface displacement induced by the shear layer instability and/or self-excited oscillations of the cavity flow. These effects can lead to the pitching moment phase jump from 0 to 180 deg during phase 2, when the body crosses the shear layer. The jump may trigger quick transition from one pitch angle trajectory to another for phase 3, when the body is outside the cavity. Our calculations showed that this interpretation is consistent with the experimental data indicating the existence of two substantially different pitching trajectories for approximately the same initial conditions. Because nonlinear dynamic equations are involved, the body trajectory may have a bifurcation point associated with phase 2. Although this transitional phase is relatively short, its aerodynamics may determine the selection between possible trajectories outside the cavity. Further theoretical and experimental studies are needed to establish and clarify the bifurcation mechanism. Our future work will extend this model to transonic speeds.

Acknowledgments

Portions of this effort were supported by the Air Force Office of Scientific Research, Air Force Materials Command, under Contract F49620-92-C-0006 and F49620-96-C-0004. The U.S. Government is authorized to reproduce and distribute reprints for government purposes, notwithstanding any copyright notation thereon. The views and conclusions herein are those of the authors and should not be interpreted as necessarily representing the official policies or endorsements, either expressed, or implied of the Air Force Office of Scientific Research or the U.S. Government.

References

[1]Goodwin, F. K., Dillenius, M. F. E., and Nielsen, J. N., "Prediction of Six-Degree-of-Freedom Store Separation Trajectories at Speeds up to the Critical Speed. V.1. Theoretical Methods and Comparison with Experiment," U.S. Air Force Flight Dynamics Lab., Dayton, OH, AFFDL-TR-72-83, Oct. 1972.

[2]Wood, M. E., "Application of Experimental Techniques to Store Release Problems," *Proceedings of Nielsen Engineering and Research Inc., Conference on Missile Aerodynamics*, Monterey, CA, 1988.

[3]Stanek, M. J., Sinha, N., Ahuja, V., and Birkbeck, R. M., "Acoustic-Compatible Active Flow Control for Optimal Weapon Separation," AIAA Paper 99-1911, 1999.

[4]Malmuth, N. D., Fedorov, A. V., Shalaev, V., Cole, J., Khokhlov, A., Hites, M., and Williams, D., "Problems in High Speed Flow Prediction Relevant to Control," AIAA Paper 98-2695, June 1998.

[5]Malmuth, N. D., Shalaev, V. I., and Fedorov, A. V., "Combined Asymptotics and Numerical Methods for Store Interactions," Final Rept., Contract F49620-96-C-0004, Air Force Office of Scientific Research/NM, Oct. 1998; available from Defense Technical Information Center [online database], URL: http//stient.dtic.mil.

[6]Cole, J. D., *Perturbation Methods in Applied Mathematics*, Waltham, MA, 1968.

[7]Hites, M., Williams, D., and Malmuth, N., "Photographic Investigation of the Dynamics of an Ogive Model Near a Cavity at Subsonic Mach Numbers," Final Rept., Fluid Dynamics Research Center, Illinois Inst. of Technology, Chicago, IL, Jan. 1998.

[8]Nielsen, J. N., *Missile Aerodynamics*, McGraw–Hill, New York, 1960.

[9]Korn, G. A., and Korn, T. M., *Mathematical Handbook,* McGraw–Hill, New York, 1968.

P. Givi
Associate Editor